Bridging art and engineering using Escher-based virtual elements

Glaucio H. Paulino · Arun L. Gain

Abstract The geometric shape of an element plays a key role in computational methods. Triangular and quadrilateral shaped elements are utilized by standard finite element methods. The pioneering work of Wachspress laid the foundation for polygonal interpolants which introduced polygonal elements. Tessellations may be considered as the next stage of element shape evolution. In this work, we investigate the topology optimization of tessellations as a means to coalesce art and engineering. We mainly focus on M.C. Escher's tessellations using recognizable figures. To solve the state equation, we utilize a Mimetic Finite Difference inspired approach, known as the Virtual Element Method. In this approach, the stiffness matrix is constructed in such a way that the displacement patch test is passed exactly in order to ensure optimum numerical convergence rates. Prior to exploring the artistic aspects of topology optimization designs, numerical verification studies such as the displacement patch test and shear loaded cantilever beam bending problem are conducted to demonstrate the accuracy of the present approach in two-dimensions.

Keywords Escher tessellations · Virtual element method · Mimetic finite difference method · Topology optimization · Density-based method

G. H. Paulino · A. L. Gain
Department of Civil and Environmental Engineering, University of Illinois at Urbana-Champaign (UIUC), Urbana, IL 61801, USA

G. H. Paulino (✉)
School of Civil and Environmental Engineering, Georgia Institute of Technology, 790 Atlantic Drive, Atlanta, GA 30332, USA
e-mail: paulino@gatech.edu

1 Introduction

Finite element analysis (FEA), in two-dimensions, typically utilize triangular and quadrilateral elements (Cook et al. 2002). However, recently polygonal elements, which are inspired from nature, have grown in stature. Such inspiration from nature is illustrated by Fig. 1, which shows that carbon allotropes, salt and basalt crystals are all polygonal (Fig. 1a). Organic cells, for instance the cells of the moss *Plagiomnium affine*, posses polygonal geometry (Fig. 1b). Beehives (Fig. 1c), pattern on the skins of tropical fish and giraffe (Fig. 1d) are also inherently polygonal in shape. Polygonal elements have been used in a wide variety of fields such as fracture mechanics (Bolander and Saito 1998; Bolander and Sukumar 2005; Bishop 2009), topology optimization (Talischi et al. 2010, 2012; Gain and Paulino 2012), micromechanical analysis (Ghosh 2011), computer graphics and image processing (Floater 2003; Hormann and Tarini 2004; Hormann and Sukumar 2008). Having explored the utility of polygonal elements in diverse fields, researchers have often pondered where do we go next? What is the next evolutionary stage of element geometries? One potential direction consists of exploring *tessellations*. A tessellation refers to the arrangement of one or more geometric shapes to completely cover the plane, without overlaps and gaps. Tessellations have the potential to bridge diverse fields such as engineering, art, mathematics and mechanics, which is the focus of investigation of the current work.

Tessellations are divisions of a plane using closed regular as well as irregular shapes. There have been many pioneers in this field. Dutch graphic artist Maurits Cornelis
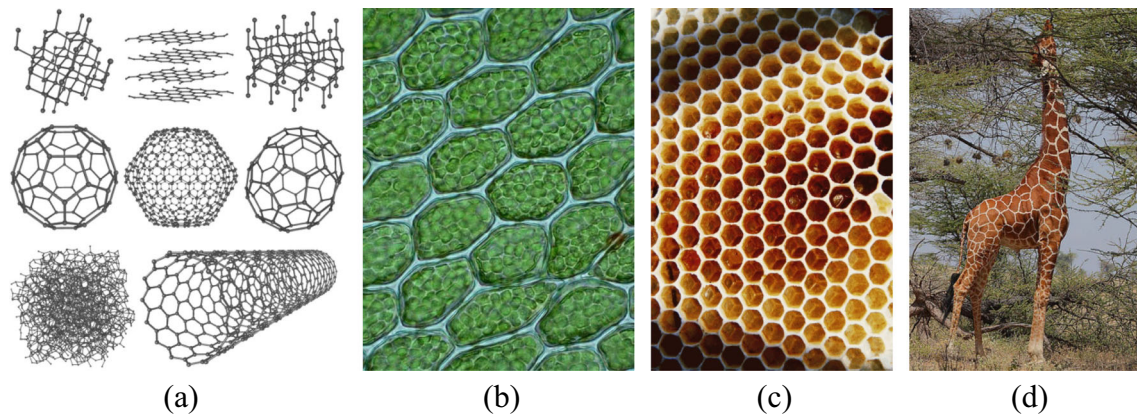
Fig. 1 Motivation behind polygonal elements. **(a)** Carbon allotropes (www.chemicool.com). **(b)** Cells of the moss *Plagiomnium affine* (http://forum.mikroscopia.com). **(c)** Beehive (http://openbydesign.wpmued.org). **(d)** Giraffe skin (www.wikipedia.org)

Escher was a prolific creator of visual riddles, impossible structures, tessellations and patterns (Escher ; Bool et al. 1992; Schattschneider 2004; Emmer and Schattschneider 2005). He is well known for his, often mathematically inspired, lithographs and woodcuts. Some of his famous works include impossible constructions and art works such as *Waterfall* and *Hand with Reflecting Sphere*. Electrical engineer Robert Fathauer is another well-known tessellation artist. He is one of the first artists who used computers to generate tessellations. He is well-known for his artwork involving fractals, knots and links (Fathauer 2010, 2011). Mathematics professor Roger Penrose is an expert in recreational math and has made significant contributions in the field of geometric puzzles and tessellations. Penrose tiles are one of his pioneering works (1979a, b). Penrose tiles are self-similar quasicrystals which possess reflective and rotational symmetry but lack translational symmetry (Fig. 2).

In order to numerically solve governing partial differential equations (PDEs) on arbitrary polygonal meshes, specialized approaches are available. The finite element method using polygonal shape functions is one such approach. The work of Wachspress (1975) on rational polygonal interpolants laid the foundations for future research in the field of polygonal interpolants (Warren 1996; Sukumar et al. 2001; Floater 2003; Floater et al. 2004; Sukumar and Tabarraei 2004; Sukumar 2004). Natural neighbor shape functions are another popular class of polygonal interpolants which can be further subcategorized as Sibson coordinates (Sibson 1980) and Non-Sibson coordinates (Belikov et al. 1997; Hiyoshi and Sugihara 1999; Christ et al. 1982; Sukumar et al. 2001; Sukumar and Tabarraei 2004). Wachspress and natural neighbor shape functions are limited to convex polygons only. The mean value coordinates developed by Floater (2003), and subsequently extended to three-dimensions (Floater et al. 2005), are well-defined for concave polygons, however they can be non-positive (Hormann and Sukumar 2008). Sukumar (2004) and Arroyo and Ortiz (2006) developed maximum entropy shape functions based on the Jaynes's principle of maximum entropy for convex polytopes. Later, Hormann and Sukumar (2008)
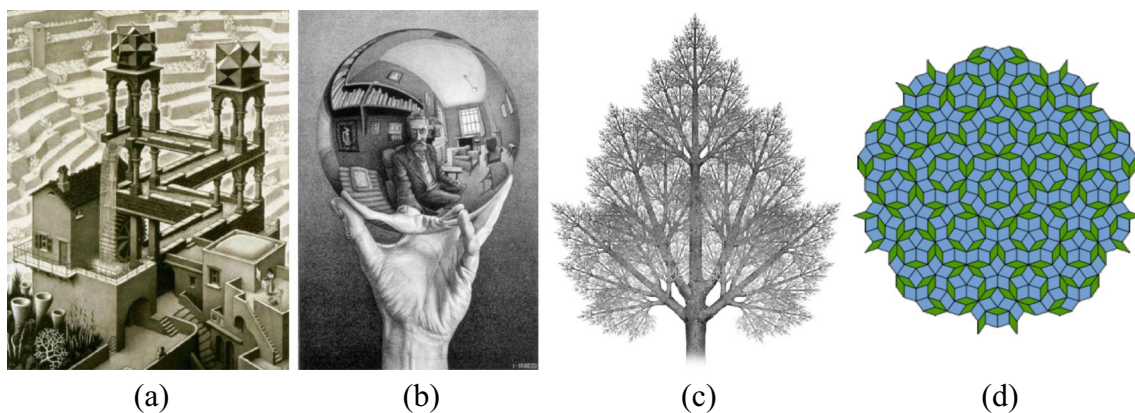

Fig. 2 Artworks of well-known artists. M.C. Escher's **(a)** Waterfall, **(b)** Hand with Reflecting Sphere (www.wikipedia.org). **(c)** Robert Fathauer's fractal tree (http://mathartfun.com). **(d)** Roger Penrose's penrose tiling (www.wikipedia.org)

extended the maximum entropy shape functions to arbitrary polytopes using prior functions. For an overview of the main developments in the field of conforming polygonal interpolants, we direct the reader to reference (Sukumar and Malsch 2006).

Polygonal shape functions-based finite element analysis typically involves transferring the weak form integration to a reference domain and using either specialized integration schemes (Natarajan et al. 2009) or subdividing the polygons in triangles/quads and using usual quadrature rules for the subdomains. Due to inexact numerical integration of weak form integrals consisting of non-polynomial shape functions, the patch test is not passed which may lead to a decay in the numerical solution convergence rate. A high-order quadrature rule is required for numerical accuracy, which is computationally inefficient and undesirable, especially for tessellations which contain large number of vertices. In this case, the numerical simulations can become cumbersome. The recently proposed approach, known as the Virtual Element Method (VEM), addresses the issue of both accuracy as well as efficiency of the underlying numerical method.

The VEM has its roots in Mimetic Finite Difference (MFD) methods. Unlike the standard finite element method (FEM), MFDs do not use explicitly defined shape functions associated with the discrete degrees of freedom. The continuous differential operators such as the div, grad and curl, are *mimicked* by their discrete counterparts that utilize the discrete quantities defined at the degrees of freedom. This feature provides great flexibility in the choice of the geometric shapes of the admissible elements. Thus, generic shaped elements based on Escher's motifs are all admissible. The distinguishing feature of VEM is that the stiffness matrix is computed directly using the projection map, which kinematically decomposes element deformation space into linear and higher-order modes. The patch test is passed because the projection map captures the linear deformation modes exactly. The VEM has been explored for two-dimensional Laplace's and Poisson's (Beirão Da Veiga et al. 2013a, c); diffusion (Beirão Da Veiga and Manzini 2013); two-dimensional (Beirão Da Veiga et al. 2013b), and three-dimensional elasticity problems (Gain et al. 2013, 2014); and plate bending problems (Brezzi and Marini 2013). Indeed, VEM provides an elegant way to handle non self-intersecting closed polygons. In this work, we use the VEM to solve the elasticity state equation for topology optimization simulations. Topology optimization aims to obtain an optimal material distribution in a domain in order to satisfy certain prescribed design objectives. Since the early works of Bendsøe and Kikuchi (1988), Suzuki and Kikuchi (1991), Bendsøe (1989), and Rozvany et al. (1992), the field of topology optimization has rapidly grown (Hassani and Hinton 1999; Bendsøe and Sigmund 2003; Christensen and Klarbring 2008; Ohsaki 2010).

Tessellations have been explored in computational mechanics in the past in the form of tilings. The terms *tiling* and *tessellation* are often used interchangeably. Tiling refers to patterns of polygons with straight boundaries. Tilings, such as the *pinwheel*, have been used in fracture mechanics (Papoulia et al. 2006; Paulino et al. 2010) because pinwheel tiling produces tiles in infinitely many orientations which is of advantage for crack propagation. *In this work, we investigate topology optimization on tessellated meshes as a means to coalesce engineering and art.*

The remainder of this paper is organized as follows. In Section 2, we discuss the generation of tessellations using basic two-dimensional shapes such as triangles and quadrilaterals. In Section 3, we briefly discuss the VEM to solve two-dimensional linear elasticity on meshes with arbitrarily shaped elements. The problem formulation of topology optimization is presented in Section 4. In Section 5, we conduct some numerical verification studies to illustrate the accuracy of the numerical approach. Section 6 shows some artistic topology optimization designs. Finally, we conclude with some remarks in Section 7.
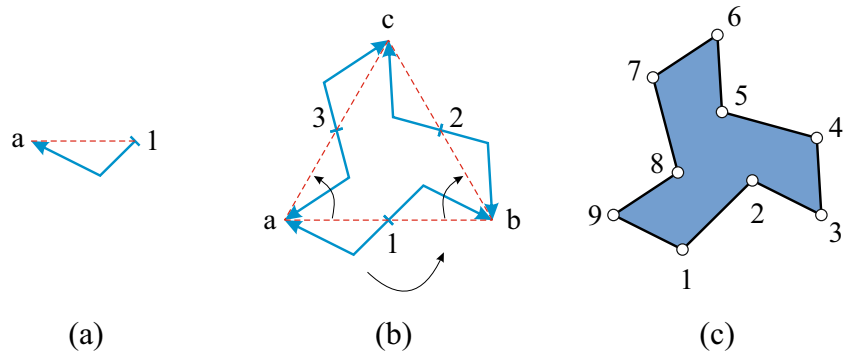
2 Tessellation generation

In this section, we discuss the generation of tessellations which we use to explore art in engineering. All the tessellations discussed here make use of basic two-dimensional shapes – triangles and quadrilaterals – as the initial background shape which is then modified to obtain the *motifs*[1] used to generate the tessellations. These tessellations are created using basic concepts of translation and rotation. The tessellations discussed in this work are divided into two categories. The first category of tessellations are created by minor modifications of the basic shapes. The second category of tessellations are based on recognizable figures such as images of birds, animals, people and other day-to-day objects, which one could relate to. These tessellations use *motifs* with very intricate straight/curved lines drawn to resemble recognizable objects. Because M.C. Escher was a great exponent of such tessellations, we employ some of his designs based on the concepts discussed in reference (Schattschneider 2004).

2.1 Tessellations of simple polygons

Starting with the triangle as the building block and using translation and rotation operations, we create four sets of

---

[1]M.C. Escher defines *motif* as a certain polygonal form that repeats itself in congruent shapes to form a tessellation (Schattschneider 2004).

(a)　　　　(b)　　　　(c)

tessellations. Figure 3 illustrates the sequence of steps to create triangle based tessellations. We start with the red dashed line **a1** and bend it into the blue solid line. The bent blue line **a1** is rotated by 180° about **1** to obtain the solid line **ab**, which is then rotated by ±60° in counter-clockwise and clockwise direction to obtain solid lines **ac** and **bc**, respectively.

By horizontally and vertically translating the patches created using the technique illustrated in Fig. 3, the tessellations in Fig. 4 are created. Each patch/element in tessellations *Tess T1* (Fig. 4a), *Tess T2* (Fig. 4b), *Tess T3* (Fig. 4c), *Tess T4* (Fig. 4d) contains 9, 15, 15 and

27 nodes, respectively. The nodes in each element are numbered counterclockwise and we conduct checks to ensure that there are no duplicate nodes in the resulting mesh.

Next, we create a few tessellations starting with quadrilaterals. The sequence of steps to generate these tessellations is similar to that for the triangular base ones discussed previously. We start from the red dashed line **a1** and bend it into the piecewise blue solid line. The bent line **a1** is rotated by 180° about **1** to obtain solid line **ab**, which is then rotated by 90° to obtain solid line **ad**. The bent blue solid lines **ab** and **ad** are translated vertically and

Fig. 4 Triangle-based tessellations generated using the patches shown in the corresponding insets at the left hand side of each figure. (**a**) *Tess T1 (9 corners)*. (**b**) *Tess T2 (15 corners)*. (**c**) *Tess T3 (15 corners)*. (**d**) *Tess T4 (27 corners)*
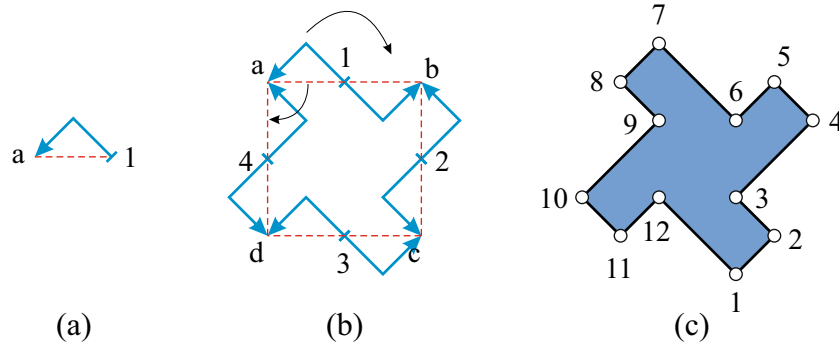

(a)　　　　(b)

(c)　　　　(d)
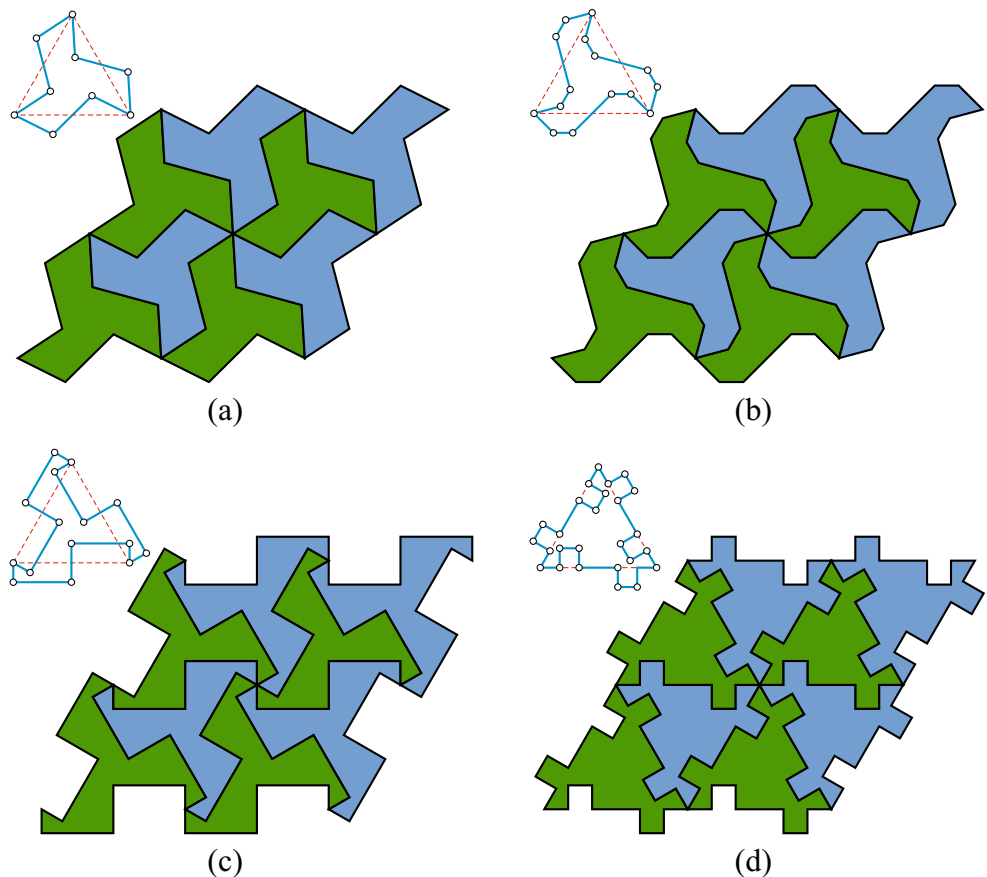
Fig. 5 Quadrilateral based tessellation generation sequence. **(a)** The red dashed line **a1** is first bend it into the piecewise blue solid line. **(b)** The blue solid line is rotated by 180° about **1** to obtain the piecewise solid line **ab**. Line **ab** is then rotated by 90° to obtain solid line **ad**. Finally, the bent blue solid lines **ab** and **ad** are translated vertically and horizontally to obtain solid lines **dc** and **bc**, respectively. **(c)** Node numbering for the resulting element

horizontally to obtain solid lines **dc** and **bc**, respectively (Fig. 5).

The tessellations in Fig. 6 are created using the technique illustrated in Fig. 5. Each patch in the tessellations shown in Fig. 6a and b contain 12 and 20 nodes, respectively.

2.2 Tessellations of recognizable figures

Dutch artist M.C. Escher pioneered the creation of tessellations using recognizable figures such as birds, horses, fishes and lizards (Schattschneider 2004). Escher classified his tessellations into quadrilateral systems and triangle systems. In his work, quadrilateral-based tessellations are more common as they are easier to work with. He further sub-categorizes his quadrilateral systems depending on two characteristics: the type of underlying polygon and the symmetry present in the *motif*. The type of the polygons are represented by letters A, B, C, D and E, denoting parallelogram, rhombus, rectangle, square and isosceles right triangle, respectively. And the Roman numerals I through X represent various symmetry types obtained by different combinations of translations, rotations and glide-reflections (reflection followed by translation) (for more details refer to Schattschneider (2004)). In this work, we will explore a few tessellations of type I^D, V^C and IV^B.

We start with the Pegasus and Bird tessellation which belong to the system of type I^D. Class I^D tessellations use a square as the underlying polygon (square **abcd** in Figs. 7 and 8) and use translation in both transversal directions and diagonal directions. Straight edges **dc** and **da** are replaced by the curved lines as shown in insets of Figs. 7 and 8. Then curved lines **dc** and **da** are translated vertically and horizontally to **ab** and **cb** to complete the *motif*. In our tessellations, we use a total of 66 and 52 nodes per Pegasus and Bird *motif*, respectively. Final tessellations are created by simply translating the *motifs*, obtained earlier, vertically and horizontally.

The Bulldog is a type V tessellation. To create the *motifs*, parallelogram **abcd** (Fig. 9) is used as the initial background shape. Straight edge **dc** represented by the red dashed line is deformed into a curved line (green colored) and is then glide-reflected (translation of the reflected image) to the bottom edge **ba**. The Bulldog *motif* is completed by

Fig. 6 Quad-based tessellations generated using the patches shown in the corresponding insets at the left hand side of each figure. **(a)** *Tess Q1 (12 corners)*. **(b)** *Tess Q2 (20 corners)*
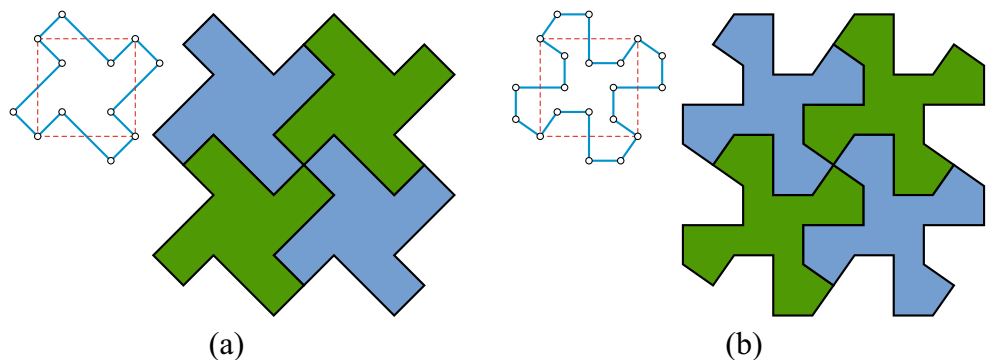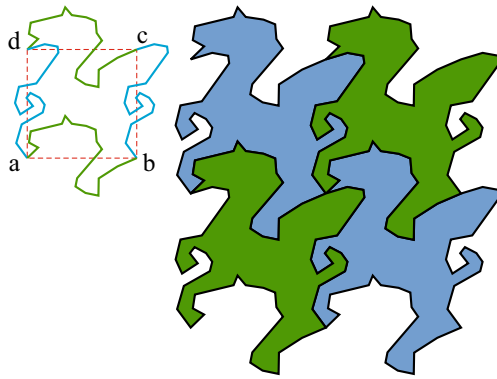
Fig. 7 The 66-corner Pegasus - Escher's tessellation of type I^D

Fig. 9 The 72-corner Bulldog - Escher's tessellation of type V^C

translating the blue curved edge **da** horizontally to edge **cb**. By repeating identical copies of this *motif* horizontally and alternating the mirror copies vertically, the Bulldog tessellation can be obtained. Escher classified this design as type V^C (Schattschneider 2004). We have 72 nodes per Bulldog element.

As an example of type IV^B, we look at the Winged Lion tessellation (Fig. 10). A quadrilateral shaped like a dart or kite is used as the starting polygon. Deformed edges **dc** and **ad** are glide-reflected to edges **cb** and **ba**, respectively to create the *motifs*. Each Winged Lion *motif* has 76 nodes.

3 On the Virtual Element Method (VEM) for two-dimensional elasticity

Current work focuses on a linearized elastic system under small deformations subjected to surface tractions t. The elasticity problem is expressed as, find u:

$$a(u, v) = f(v), \qquad \forall u, v \in \mathcal{V} \tag{1}$$

where

$$a(u, v) = \int_{\Omega} C \epsilon(u) : \epsilon(v) \, dx, \qquad f(v) = \int_{\Gamma_t} t \cdot v \, ds \tag{2}$$

$$\mathcal{V} = \left\{ v \in H^1 (\Omega)^2 : v|_{\Gamma_u} = 0 \right\}$$

where $\epsilon(u)$ is the second-order linearized strain tensor (symmetric part of the gradient of u) and C is the elasticity tensor. For the topology optimization problem, we define the design domain, Ω, to contain all admissible shapes ω, i.e., $\omega \subseteq \Omega$. Its boundary $\partial\Omega$ consists of three disjoint segments, $\partial\Omega = \Gamma_u \cup \Gamma_{t0} \cup \Gamma_t$, where Γ_u, Γ_{t0}, and Γ_t represent displacement, homogeneous traction, and non-homogeneous traction boundary conditions ($t \neq 0$), respectively. Also, the design ω, with boundary $\partial\omega = \gamma_u \cup \gamma_{t0} \cup \gamma_t$, is constrained to satisfy $\gamma_u \subseteq \Gamma_u$ and $\gamma_t = \Gamma_t$. Here, γ_u, γ_{t0}, and γ_t correspond to the boundaries of ω with displacement, homogeneous traction, and non-homogeneous traction boundary conditions, respectively (c.f. Fig 11). The body forces are ignored. In this work, we shall denote the components of vectors, matrices and tensors in the canonical Euclidean basis with subscripts inside parentheses (e.g. $u_{(i)}$ or $\epsilon_{(ij)}$) in order to make a distinction with indexed quantities.

In order to numerically solve the governing elasticity (1) for topology optimization, we use the Virtual Element Method (VEM) (Beirão Da Veiga et al. 2013b; Gain et
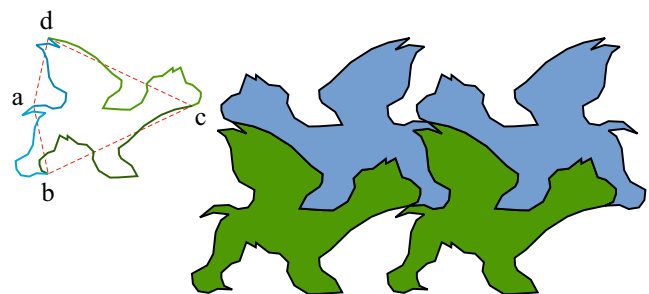

Fig. 8 The 52-corner - Escher's tessellation of type I^D

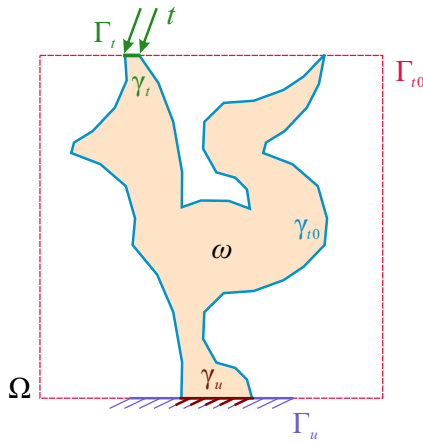**Fig. 10** The 76-corner Winged Lion - Escher's tessellation of type IV^B

Fig. 11 Illustration of the design domain, Ω. Its boundary, $\partial\Omega$, contains three disjoint segments, $\partial\Omega = \Gamma_u \cup \Gamma_{t0} \cup \Gamma_t$, corresponding to displacement, homogeneous traction, and non-homogeneous traction boundary conditions, respectively. Any design $\omega \subseteq \Omega$, with boundary $\partial\omega = \gamma_u \cup \gamma_{t0} \cup \gamma_t$, is constrained to satisfy $\gamma_u \subseteq \Gamma_u$ and $\gamma_t = \Gamma_t$. Boundaries $\gamma_u, \gamma_{t0},$ and γ_t correspond to displacement, homogeneous traction, and non-homogeneous traction boundary conditions on $\partial\omega$, respectively

al. 2013, 2014). Here, we discuss the method for two-dimensional linear elasticity. We begin with partitioning the design domain Ω into disjoint non-overlapping generic polygons, e, of maximum diameter h. The Galerkin approximation u_h of u belongs to the conforming discrete space $\mathcal{V}_h \subseteq \mathcal{V}$ which consists of continuous displacement fields whose restriction to polygon e belongs to the finite-dimensional space of smooth functions $\mathcal{W}$. Space $\mathcal{W}$ contains all the deformation states of element e - linear deformations and higher-order modes. The continuous (a) and discrete bilinear form (a_h) can be expressed as the corresponding sums of element contributions due to the conformity of $\mathcal{V}_h$ as:

$$a(\boldsymbol{u}, \boldsymbol{v}) = \sum_e a^e(\boldsymbol{u}, \boldsymbol{v}), \qquad a_h(\boldsymbol{u}, \boldsymbol{v}) = \sum_e a_h^e(\boldsymbol{u}, \boldsymbol{v}) \quad (3)$$

To construct the space $\mathcal{W}$ two degrees of freedom are associated with each vertex of a polygon. Therefore, we consider the canonical basis $\boldsymbol{\varphi}_1, \ldots, \boldsymbol{\varphi}_{2n}$ of the form

$$\boldsymbol{\varphi}_{2i-1} = [\varphi_i, \, 0]^T, \quad \boldsymbol{\varphi}_{2i} = [0, \, \varphi_i]^T, \quad i = 1, \ldots, n \quad (4)$$

where $\varphi_1, \ldots, \varphi_n$ are a set of *barycentric coordinates* (Wachspress 1975; Sukumar et al. 2001; Floater 2003), which satisfy all the desired properties of a conforming interpolants such as partition of unity, linear completeness, Kronecker-delta and piece-wise linear (C^0 function) along the edges of e. As we shall see later, the VEM concerns only with the behavior of $\mathcal{W}$ along the boundaries of the element e.

In VEM, we do not compute the shape functions, rather the stiffness matrix is constructed directly based on the kinematic decomposition of the deformation states of the space of smooth functions $\mathcal{W}$. To simplify the expressions, the mean of the values of a function $\boldsymbol{v}$ sampled at the vertices of e and area average of $\boldsymbol{v}$ are represented by $\overline{\boldsymbol{v}}$ and $\langle \boldsymbol{v} \rangle$, respectively. We define six bases that span the space of linear deformations, $\mathcal{P}$, over element e as:

$$\begin{aligned}
\boldsymbol{p}_1(\boldsymbol{x}) &= [1, 0], & \boldsymbol{p}_4(\boldsymbol{x}) &= \left[(\boldsymbol{x} - \overline{\boldsymbol{x}})_{(2)}, 0\right], \\
\boldsymbol{p}_2(\boldsymbol{x}) &= [0, 1], & \boldsymbol{p}_5(\boldsymbol{x}) &= \left[0, (\boldsymbol{x} - \overline{\boldsymbol{x}})_{(1)}\right], \\
\boldsymbol{p}_3(\boldsymbol{x}) &= \left[(\boldsymbol{x} - \overline{\boldsymbol{x}})_{(1)}, 0\right], & \boldsymbol{p}_6(\boldsymbol{x}) &= \left[0, (\boldsymbol{x} - \overline{\boldsymbol{x}})_{(2)}\right].
\end{aligned}$$
$$(5)$$

Next, we define a projection map $\pi_{\mathcal{P}} : \mathcal{W} \to \mathcal{P}$ to extract linear deformations as:

$$\pi_{\boldsymbol{P}} \boldsymbol{v} = \overline{\boldsymbol{v}} + \langle \nabla \boldsymbol{v} \rangle (\boldsymbol{x} - \overline{\boldsymbol{x}}) \quad (6)$$

We observe that the area integral $\langle \nabla \boldsymbol{v} \rangle$ can be converted to line integral as follows:

$$\langle \nabla \boldsymbol{v} \rangle = \frac{1}{|e|} \int_e \nabla \boldsymbol{v} \, d\boldsymbol{x} = \frac{1}{|e|} \int_{\partial e} \boldsymbol{v} \otimes \boldsymbol{n} \, d\boldsymbol{s}, \quad (7)$$

which can be computed exactly as the function $\boldsymbol{v}$ is assumed linear along the edges. Also, the linear projection map $\pi_{\mathcal{P}}$ can be expressed in terms of the bases of $\mathcal{P}$ as:

$$\begin{aligned}
\pi_{\mathcal{P}} \boldsymbol{v} = &(\overline{\boldsymbol{v}})_{(1)} \boldsymbol{p}_1 + (\overline{\boldsymbol{v}})_{(2)} \boldsymbol{p}_2 + \langle \nabla \boldsymbol{v} \rangle_{(11)} \boldsymbol{p}_3 \quad (8) \\
&+ \langle \nabla \boldsymbol{v} \rangle_{(12)} \boldsymbol{p}_4 + \langle \nabla \boldsymbol{v} \rangle_{(21)} \boldsymbol{p}_5 + \langle \nabla \boldsymbol{v} \rangle_{(22)} \boldsymbol{p}_6
\end{aligned}$$

Note that in order to ensure consistency of the approach, $\pi_{\mathcal{P}}$ is defined such that $(\boldsymbol{v} - \pi_{\mathcal{P}} \boldsymbol{v})$ is *energetically* orthogonal to $\mathcal{P}$, $\forall \boldsymbol{v} \in \mathcal{W}$, i.e. $a^e(\boldsymbol{p}, \boldsymbol{v} - \pi_{\mathcal{P}} \boldsymbol{v}) = 0, \forall \boldsymbol{p} \in \mathcal{P}$. Finally, any deformation state $\boldsymbol{v} \in \mathcal{W}$ can be kinematically decomposed as:

$$\boldsymbol{v} = \pi_{\mathcal{P}} \boldsymbol{v} + (\boldsymbol{v} - \pi_{\mathcal{P}} \boldsymbol{v}) \quad (9)$$

where $(\boldsymbol{v} - \pi_{\mathcal{P}} \boldsymbol{v})$ represents the higher-order component that belongs to a $(2n - 6)$ dimensional subspace of $\mathcal{W}$.

Based on the kinematic decomposition of deformation state and the energy orthogonality property, the continuous bilinear form can be written as:

$$a^e(\boldsymbol{u}, \boldsymbol{v}) = a^e(\pi_{\mathcal{P}} \boldsymbol{u}, \pi_{\mathcal{P}} \boldsymbol{v}) + a^e(\boldsymbol{u} - \pi_{\mathcal{P}} \boldsymbol{u}, \boldsymbol{v} - \pi_{\mathcal{P}} \boldsymbol{v}) \quad (10)$$

The first term corresponds to the constant strain modes and can be computed exactly by knowing the area of the element e (note that the arguments of the bilinear term are linear). This ensures that the engineering patch test is passed. The second term, corresponding to higher-order deformation modes, is difficult to compute. We replace this term by a crude estimate s^e, which can be conveniently computed, without affecting the energy associated with the constant strain modes. Thus, the discrete bilinear form is defined as:

$$a^e(\boldsymbol{u}, \boldsymbol{v}) \doteq a^e(\pi_{\mathcal{P}} \boldsymbol{u}, \pi_{\mathcal{P}} \boldsymbol{v}) + s^e(\boldsymbol{u} - \pi_{\mathcal{P}} \boldsymbol{u}, \boldsymbol{v} - \pi_{\mathcal{P}} \boldsymbol{v}) \quad (11)$$

where s^e is any symmetric positive definite bilinear form chosen such that it has similar energy as the consistency term, $s^e(\cdot, \cdot) = a^e(\cdot, \cdot)$. We make a computationally inexpensive choice as Beirão Da Veiga et al. (2013a):

$$s^e(\boldsymbol{u}, \boldsymbol{v}) = \sum_{i=1}^{n} \alpha^e \boldsymbol{u}(\boldsymbol{x}_i) \cdot \boldsymbol{v}(\boldsymbol{x}_i) \tag{12}$$

where α^e is a positive coefficient that ensures correct scaling of the energies of higher-order modes.

For implementing the above approach, we proceed as follows. Let $\boldsymbol{P}_{\mathcal{P}}$ be the discrete representation of the projection $\pi_{\mathcal{P}}$, i.e.,

$$\pi_{\mathcal{P}} \boldsymbol{\varphi}_j = \sum_{k=1}^{2n} (\boldsymbol{P}_{\mathcal{P}})_{(kj)} \boldsymbol{\varphi}_k \tag{13}$$

To obtain $\boldsymbol{P}_{\mathcal{P}}$, we use (8) to express $\pi_{\mathcal{P}}$ in terms of the bases that span the linear deformation space as:

$$\pi_{\mathcal{P}} \boldsymbol{\varphi}_j = \sum_{\ell=1}^{6} (\boldsymbol{W}_{\mathcal{P}})_{(j\ell)} \boldsymbol{p}_\ell \tag{14}$$

where $\boldsymbol{W}_{\mathcal{P}}$ is an $2n \times 6$ matrix whose jth row is given by,

$$[(\overline{\boldsymbol{\varphi}_j})_{(1)}, \ (\overline{\boldsymbol{\varphi}_j})_{(2)}, \ \langle\nabla\boldsymbol{\varphi}_j\rangle_{(11)},$$
$$\langle\nabla\boldsymbol{\varphi}_j\rangle_{(12)}, \langle\nabla\boldsymbol{\varphi}_j\rangle_{(21)}, \langle\nabla\boldsymbol{\varphi}_j\rangle_{(22)}] \tag{15}$$

Using the linear precision property of the canonical basis functions (4), we express $\boldsymbol{p}_\ell$ in (14) in terms of its discrete counterpart (bases sampled at the vertices) and upon simplification, we obtain:

$$\pi_{\mathcal{P}} \boldsymbol{\varphi}_j = \sum_{k=1}^{2n} \left(\boldsymbol{N}_{\mathcal{P}} \boldsymbol{W}_{\mathcal{P}}^T\right)_{(kj)} \boldsymbol{\varphi}_k \tag{16}$$

By comparing (16) with (13), we get $\boldsymbol{P}_{\mathcal{P}} = \boldsymbol{N}_{\mathcal{P}} \boldsymbol{W}_{\mathcal{P}}^T$, where $\boldsymbol{N}_{\mathcal{P}}, \boldsymbol{W}_{\mathcal{P}} \in \mathbb{R}^{2n \times 6}$. A block of three rows of $\boldsymbol{N}_{\mathcal{P}}$, corresponding to ith vertex of element e, is explicitly expressed as:

$$(\boldsymbol{N}_{\mathcal{P}})_{(2i-1:2i,:)} =$$
$$\begin{bmatrix} 1 & 0 & (\boldsymbol{x}_i - \overline{\boldsymbol{x}})_{(1)} & (\boldsymbol{x}_i - \overline{\boldsymbol{x}})_{(2)} & 0 & 0 \\ 0 & 1 & 0 & 0 & (\boldsymbol{x}_i - \overline{\boldsymbol{x}})_{(1)} & (\boldsymbol{x}_i - \overline{\boldsymbol{x}})_{(2)} \end{bmatrix} \tag{17}$$

and a block of three rows of $\boldsymbol{W}_{\mathcal{P}}$ is expressed as:

$$(\boldsymbol{W}_{\mathcal{P}})_{(2i-1:2i,:)} =$$
$$\begin{bmatrix} 1/n & 0 & (\boldsymbol{q}_i)_{(1)} & (\boldsymbol{q}_i)_{(2)} & 0 & 0 \\ 0 & 1/n & 0 & 0 & (\boldsymbol{q}_i)_{(1)} & (\boldsymbol{q}_i)_{(2)} \end{bmatrix} \tag{18}$$
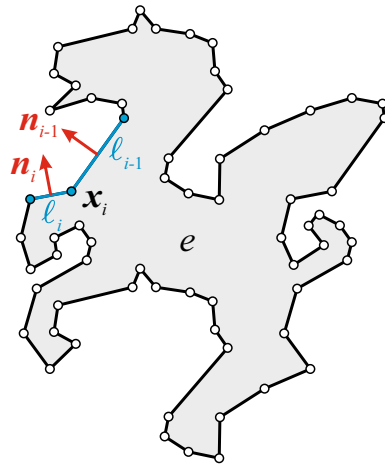

Fig. 12 Illustration of the adjacency information needed in evaluation of line integral in the VEM consistency term for an element e. Lengths of the sides adjacent to vertex $\boldsymbol{x}_i$ are represented by ℓ_{i-1}, ℓ_i. The arrows represent the outward pointing normals, $\boldsymbol{n}_{i-1}, \boldsymbol{n}_i$

where the line integral vector $\boldsymbol{q}_i$ can be computed exactly as below (c.f. Fig. 12):

$$\boldsymbol{q}_i = \frac{1}{|e|} \int_{\partial e} \varphi_i \boldsymbol{n} \mathrm{d}s = \frac{1}{|e|} (\ell_{i-1} \boldsymbol{n}_{i-1} + \ell_i \boldsymbol{n}_i) \tag{19}$$

Using the matrices $\boldsymbol{W}_{\mathcal{P}}$ and $\boldsymbol{P}_{\mathcal{P}}$, the element stiffness matrix $\boldsymbol{K}_e$ can now be computed. From (11) we have,

$$\begin{aligned} (\boldsymbol{K}_e)_{(jk)} &= a_h^e(\boldsymbol{\varphi}_j, \boldsymbol{\varphi}_k) \\ &= a^e(\pi_{\mathcal{P}}\boldsymbol{\varphi}_j, \pi_{\mathcal{P}}\boldsymbol{\varphi}_k) + s^e(\boldsymbol{\varphi}_j - \pi_{\mathcal{P}}\boldsymbol{\varphi}_j, \boldsymbol{\varphi}_k - \pi_{\mathcal{P}}\boldsymbol{\varphi}_k) \end{aligned} \tag{20}$$

Utilizing (14), the first term of $\boldsymbol{K}_e$ can be simplified as:

$$a^e(\pi_{\mathcal{P}}\boldsymbol{\varphi}_j, \pi_{\mathcal{P}}\boldsymbol{\varphi}_k) = |e| \left(\boldsymbol{W}_{\mathcal{P}} \boldsymbol{D} \boldsymbol{W}_{\mathcal{P}}^T\right)_{(jk)} \tag{21}$$

where the matrix $\boldsymbol{D}$ is a function of elasticity tensor $\boldsymbol{C}$ and is given by:

$$(\boldsymbol{D})_{(\ell m)} = \frac{1}{|e|} a^e(\boldsymbol{p}_\ell, \boldsymbol{p}_m) = \boldsymbol{C}\boldsymbol{\epsilon}(\boldsymbol{p}_\ell) : \boldsymbol{\epsilon}(\boldsymbol{p}_m),$$
$$\ell, m = 1, \ldots, 6 \tag{22}$$

Based on the inexpensive choice of s^e (12), the second term in the stiffness matrix is written as:

$$s^e(\boldsymbol{\varphi}_j - \pi_{\mathcal{P}}\boldsymbol{\varphi}_j, \boldsymbol{\varphi}_k - \pi_{\mathcal{P}}\boldsymbol{\varphi}_k) = \left[(\boldsymbol{I} - \boldsymbol{P}_{\mathcal{P}})^T \boldsymbol{S}^e (\boldsymbol{I} - \boldsymbol{P}_{\mathcal{P}})\right]_{(jk)} \tag{23}$$

where $(\boldsymbol{S}^e)_{(jk)} = s^e(\boldsymbol{\varphi}_j, \boldsymbol{\varphi}_k)$ and corresponds to $\boldsymbol{S}^e = \alpha^e \boldsymbol{I}_{2n}$. We need to ensure that $s^e(\cdot, \cdot)$ is of the same order of magnitude as $a^e(\cdot, \cdot)$, so an appropriate value of α^e is, for example

$$\alpha^e = \bar{\alpha}^e \mathrm{trace}(|e| \boldsymbol{W}_{\mathcal{P}} \boldsymbol{D} \boldsymbol{W}_{\mathcal{P}}^T) \tag{24}$$

A constant $\bar{\alpha}^e$ is chosen as 1.0. Recommendations on the optimal choice of $\bar{\alpha}^e$ can be found in reference (Gain et al. 2014). Finally, the element stiffness matrix is given by

$$K_e = |e| W_{\mathcal{P}} D W_{\mathcal{P}}^T + \alpha^e (I - P_{\mathcal{P}})^T (I - P_{\mathcal{P}}) \qquad (25)$$

To compute the force vector corresponding to a surface traction, a first-order accurate scheme, similar to the one discussed in Gain et al. (2014), can be used. The global stiffness matrix and global force vector are obtain by standard finite element assembly process (Cook et al. 2002).

4 Topology optimization

Topology optimization on tessellations is our tool for creating artistic and mechanically sound designs. We utilize topology optimization problem of compliance minimization to illustrate the artistic aspects in engineering designs. Compliance minimization problem refers to finding the stiffest configuration under the applied loads and boundary conditions. The optimization problem can be expressed as:

$$\inf_{\rho} J(\rho) = \int_{\Gamma_t} t \cdot u \, ds = \int_{\Omega} C(\rho) \epsilon(u) : \epsilon(u) \, dx$$

$$\text{s.t:} \quad a(u, v) = f(v), \qquad \int_{\Omega} \rho(x) \, dx \leq V_f |\Omega| \qquad (26)$$

where V_f is the prescribed maximum volume fraction and $|\cdot|$ denotes the measure of a set (area) as well as the Euclidean norm of vector. The effective elasticity tensor C for the domain Ω is a function of density $\rho(x)$ and, as per the Solid Isotropic Material with Penalization (SIMP) model (Bendsøe 1989; Rozvany et al. 1992), is expressed as:

$$C(\rho) = \left[\varepsilon + (1 - \varepsilon) \rho^p \right] C^0 \qquad (27)$$

The solid and void regions are filled with material of elasticity tensor C^0 and εC^0, respectively, where ε is chosen as 10^{-4}. The penalization parameter, p, is set to 3. In order to solve (26) numerically, it is discretized as follows:

$$\inf_{\rho} J = F^T U$$
$$\text{s.t:} \quad K(\rho) U = F, \qquad \sum_e |e| \rho_e \leq V_f |\Omega| \qquad (28)$$

where K, U and F are the global stiffness matrix, global nodal displacement vector and global nodal force vector, respectively.

We use gradient-based optimization algorithm and employ the Optimality Criteria (OC)[2] (Bendsøe and Sigmund 2003; Talischi et al. 2012) for solving the discrete problem (28). For our OC implementation we begin by linearizing the objective function in terms of exponential intermediate variables and approximating the constraints linearly in terms of the design variables. Utilizing the condition of optimality and subsequently solving the dual problem, we obtain the updating expression and we use reciprocal approximation which is generally used for compliance minimization (see, for example, Groenwold and Etman (2008)). Using the adjoint method (Bendsøe and Sigmund 2003) the sensitivity of J with respect to the design variable (element density, ρ_e), needed in OC, is computed as shown below:

$$\frac{\partial J}{\partial \rho_e} = -p(1 - \epsilon) \rho_e^{p-1} u_e^T K_e u_e \qquad (29)$$

Here, u_e, K_e are the element displacement vector and element stiffness matrix, respectively. Also, the sensitivity of the volume constraint (shown in (28)) with respect to element density is the element area $|e|$.

5 Numerical verification studies

In this section we verify the accuracy of the present numerical approach using the displacement patch test and shear loaded cantilever beam bending problems. The purpose of the numerical verification studies is to show that the current approach produces numerically convergent and stable results for tessellations of arbitrary shape including concave elements. The accuracy and convergence of the numerical results are verified in terms of two error measures. The relative displacement error is the first metric and is expressed as:

$$e_u = \frac{|u - u_h|}{|u|} \qquad (30)$$

where u and u_h are the exact and VEM solutions, respectively. We also define a discrete error measure for stress field as follows:

$$e_\sigma \doteq \frac{\|\sigma(u) - \sigma_h(u_h)\|_{0,\Omega}}{\|\sigma(u)\|_{0,\Omega}} \qquad (31)$$

---

[2]Other mathematical programming algorithms such as, Method of Moving Asymptotes (MMA) (Svanberg 1987), Sequential Quadratic Programming (SQP) may also be used.

Fig. 13 Displacement patch test on triangle based tessellations (**a**) *Tess T2*, (**b**) *Tess T3*. Blue colored mesh with circular nodes represents the initial configuration and red colored mesh with triangular nodes represents the deformed configuration
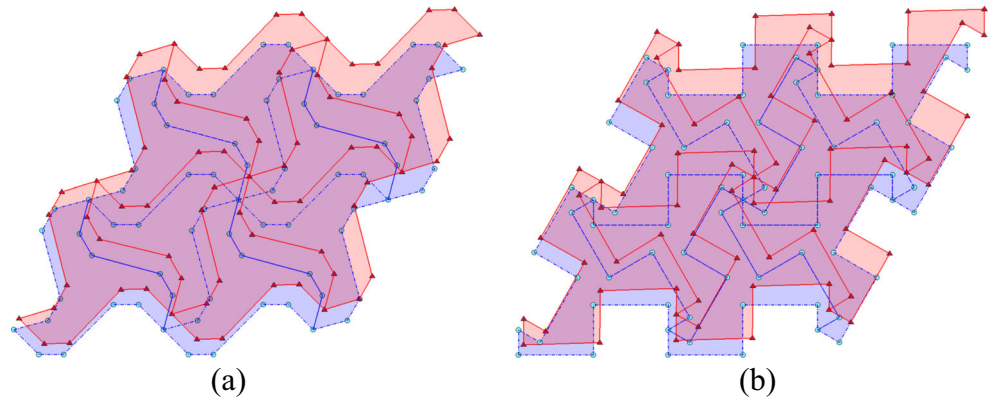
where $\boldsymbol{\sigma}_h(\boldsymbol{u}_h)$ is the element-wise constant stress (continuous field $\boldsymbol{\sigma}(\boldsymbol{u}_h)$ is not available) and for any $\boldsymbol{v} \in \mathcal{W}$ is computed as:

$$
\begin{aligned}
\boldsymbol{\sigma}_h(\boldsymbol{v})|_e &= \frac{1}{|e|} \int_e \boldsymbol{\sigma}(\boldsymbol{v}) \mathrm{d}\boldsymbol{x} = \boldsymbol{\sigma}(\pi_{\mathcal{P}}\boldsymbol{v}) \\
&= \sum_{\ell=1}^{6} [\boldsymbol{W}_{\mathcal{P}}^{\top} \boldsymbol{\chi}(\boldsymbol{v})]_\ell \boldsymbol{\sigma}(\boldsymbol{p}_\ell)
\end{aligned}
\tag{32}
$$

To numerically evaluate the integrals, we triangulate each element and use a high order quadrature rule of linear triangular elements. In this work, plane stress elasticity model is used for all the numerical studies.

5.1 Displacement patch test

We conduct the displacement patch tests for all the tessellations shown in Section 2. An arbitrary linear displacement of the form $\boldsymbol{p} \in \mathcal{P}(\Omega)$ is applied to the entire boundary $\partial\Omega$ and $\Gamma_t = \emptyset$. The exact solution for the patch test is $\boldsymbol{u} = \boldsymbol{p}$. Scaling constant $\bar{\alpha}^e \in [10^{-3} - 10^3]$ is investigated. For all tessellations, the relative displacement and stress errors are in the machine precision range (10^{-16}) indicating that for VEM the displacement patch test is passed. Our tests indicate that the choice of the scaling constant has no impact on the patch test results. Figure 13 illustrates the deformed configurations from the patch test for the triangle based tessellations *Tess T2* and *Tess T3*.
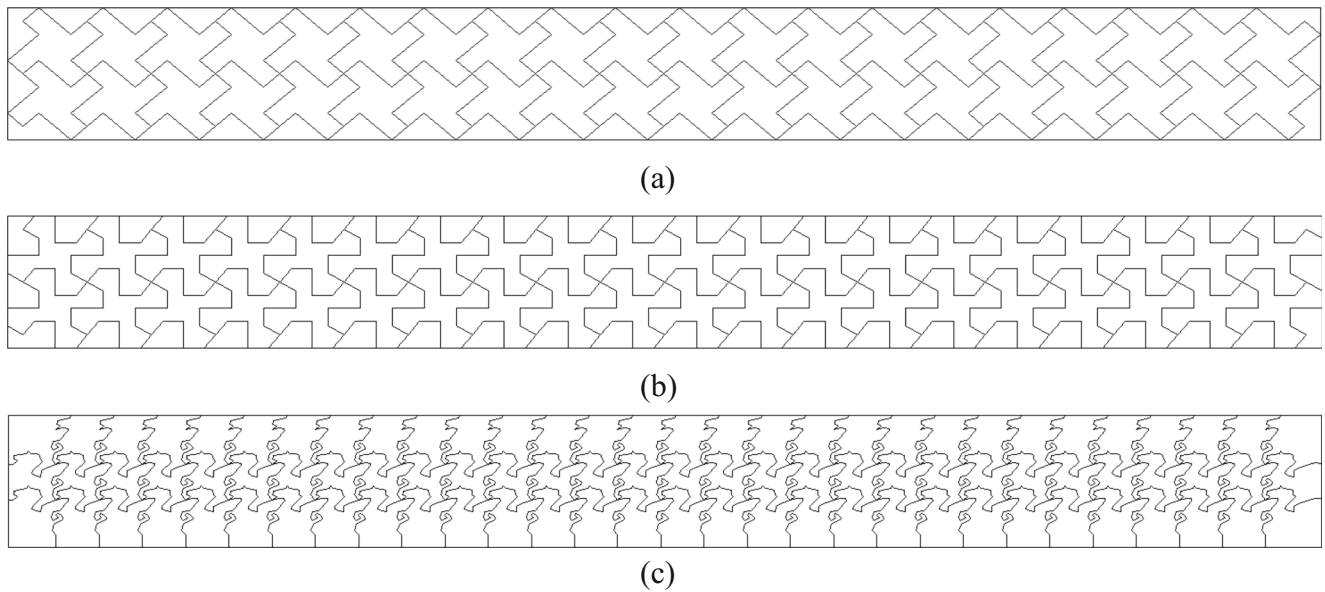

Fig. 14 Sample meshes for shear loaded cantilever beam bending problem. (**a**) *Tess Q1*, (**b**) *Tess Q2*, (**c**) *Pegasus*
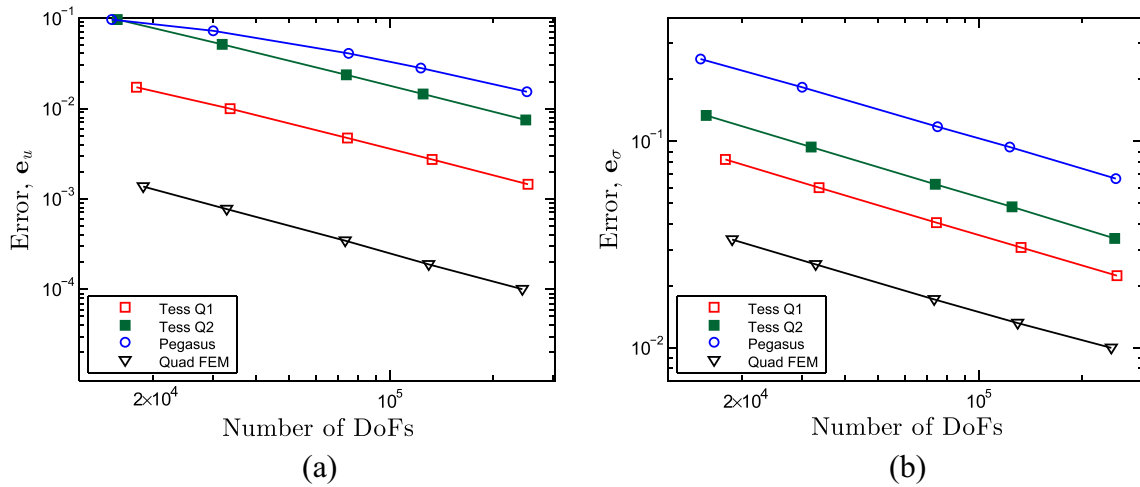
Fig. 15 Plot of error versus number of degrees of freedom *(DoFs)* for tessellations *Tess Q1*, *Tess Q2*, Pegasus using VEM and uniform quad mesh using FEM. **(a)** Displacement error, $\mathbf{e_u}$. **(b)** Stress error, $\mathbf{e_\sigma}$

### 5.2 Shear loaded cantilever beam bending

Next, we study the performance of the present numerical approach using the shear loaded cantilever beam bending problem for different tessellations. Consider a rectangular beam of dimensions $(-1, 1) \times (0, L)$ filled with isotropic material of Young's modulus E and Poisson's ration ν, subjected to transverse shear load, $\mathbf{t} = [0, -F]$, at end $\mathbf{x}_{(1)} = 0$. For the current study, $L = 20$, $F = 0.1$, $E = 1$ and $\nu = 0.3$. The expressions for stresses are available in Timoshenko and Goodier (1970) and Barber (2010) and are repeated here for completeness.

$$\boldsymbol{\sigma}_{(11)} = \frac{3F\mathbf{x}_{(1)}\mathbf{x}_{(2)}}{2}, \quad \boldsymbol{\sigma}_{(22)} = 0, \quad \boldsymbol{\sigma}_{(12)} = \frac{3F\left(1 - \mathbf{x}_{(2)}^2\right)}{4}.$$
(33)

Using the stress-strain relationships and definitions of displacement gradients, the displacement fields corresponding to the stresses (33), up to the addition of rigid body motion, can be computed as:

$$\mathbf{u}_{(1)} = \frac{3F\mathbf{x}_{(1)}^2\mathbf{x}_{(2)}}{4E} + \frac{3F(1+\nu)\mathbf{x}_{(2)}}{2E} - \frac{F(2+\nu)\mathbf{x}_{(2)}^3}{4E},$$

$$\mathbf{u}_{(2)} = -\frac{3F\nu\mathbf{x}_{(1)}\mathbf{x}_{(2)}^2}{4E} - \frac{F\mathbf{x}_{(1)}^3}{4E}.$$
(34)

Fig. 16 Bracing system design. **(a)** Problem description. **(b)** Representative Bulldog tessellation
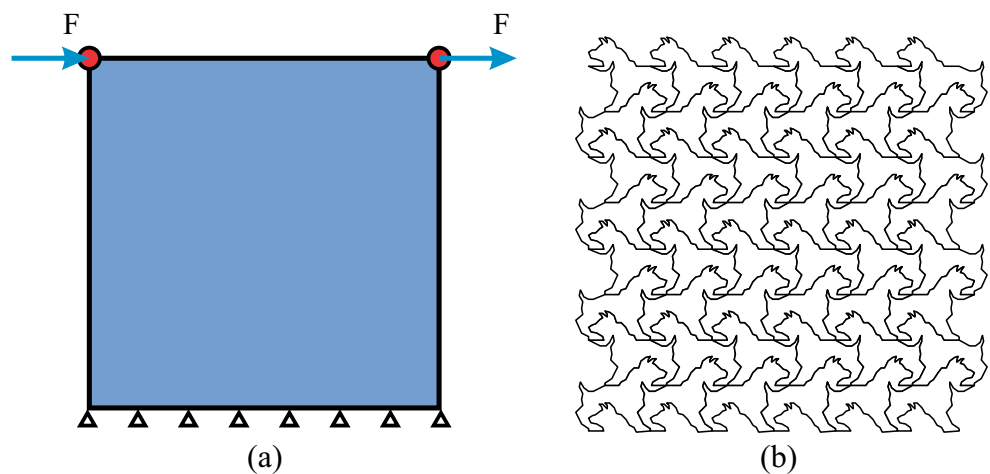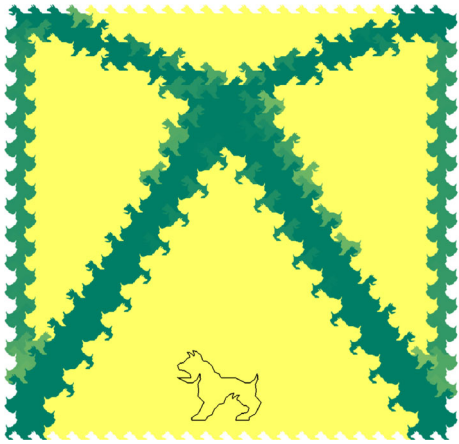
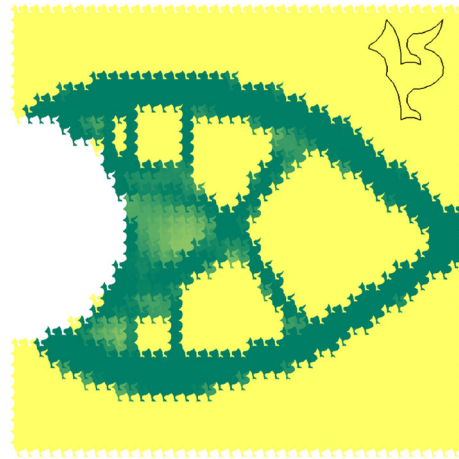**Fig. 17** Structurally efficient and aesthetically pleasing bracing design using Bulldog tessellation

Fig. 19 Converged topologies for the cantilever beam with circular support solved on Bird tessellation. The volume fraction is chosen as 0.3 and no filter is used

We studied the performance of VEM under mesh refinement for different types of tessellations shown in Fig. 14. Figure 15 shows the results of this study. In the plots, the relative displacement and stress errors are plotted against total number of degrees of freedom (DoFs). We see from Fig. 15 that under mesh refinement displacements and stresses converge for different tessellations. This confirms that skewed and non-convex elements can be accurately handled by VEM.

6 Generation of optimal and artistic designs

The goal of the current work of topology optimization on tessellated meshes is to provide a natural means to integrate artistic aspects in engineering. We illustrate this idea using three optimization examples - a bracing system design, a cantilever beam with circular support and a bridge problem. Optimization is terminated when either the maximum of the change in element densities is less than 0.01 or the maximum number of iterations exceed 150.

6.1 Bracing system design

We start with the design of practical systems, the bracings. In buildings, they provide lateral resistance to withstand loadings such as the wind and seismic forces. We consider a model problem shown in Fig. 16a. Nodes along the bottom edge are fixed and lateral loads are applied at the top

Fig. 18 Cantilever beam with circular support. **(a)** Problem description. **(b)** Representative Bird tessellation
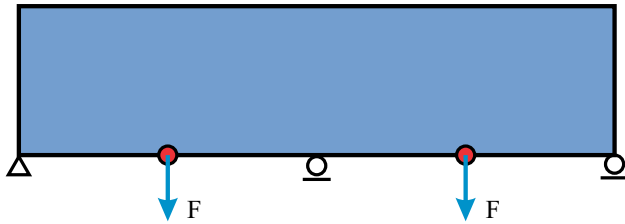

(a)

(b)
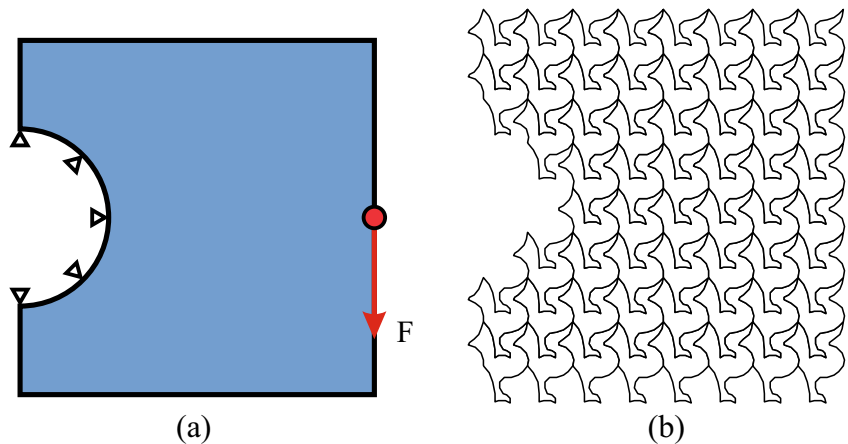
Fig. 20 Problem description for the bridge design

corners. The design domain is discretized using Escher's type V^C tessellation - Bulldog, consisting of 690 elements and 25,063 nodes. A linear filter of radius equal to 3 % of the maximum domain dimension is adopted along with a volume fraction of 0.3.

As expected, the optimization algorithm produces an X-bracing system (Fig. 17) to resist lateral loads as one would expect (Mijar et al. 1998). In this work, we are more interested in the details around the boundaries of the members. We can identify the outline of the Bulldogs and their graded pattern which add an artistic touch to an otherwise bland engineering design. To design bracing systems for high-rise buildings, manufacturing and layout constraints such as pattern repetition and pattern gradation can be employed (Almeida et al. 2010; Beghini et al. 2014). In pattern repetition manufacturing constraint utilizes the same design pattern for multiple stories to help increase the speed of construction and ensure high quality. Pattern gradation can be used for a smooth transition of the design between two dissimilar loading resistance requirements, such as for tall building where overturning

moments are higher at the bottom and shear is dominant at the top.

6.2 Cantilever beam with circular support

Next example focuses on the benchmark problem of a cantilever beam with circular support (Talischi et al. 2010). The problem description is shown in Fig. 18a. All the nodes along the circular segment are fixed and a point load, acting in the negative $x_{(1)}$-direction, is applied approximately in the middle of the right edge. The domain is discretized using Escher's type I^D tessellations - Bird (Fig. 8). The tessellation contains 1,442 elements (37,261 nodes). The volume fraction is chosen as 0.3.

First, optimization is performed without using any filters. As illustrated in Fig. 19 the overall converged topologies are similar to the ones available in the literature (Talischi et al. 2010). As before, in Fig. 19, outlines of the Bird are clearly visible and their heads and feet are well defined. Aesthetically, such designs are appealing to the architecture and fine arts communities.

In the previous designs (Fig. 19), we see that, due to the absence of filters, the boundaries, in general, are distinct. Artistically, it would be more attractive if there were a gradation at the boundaries, with elements of varying densities. To obtain such a design, we optimize the cantilever beam employing a linear filter of radius equal to 3% of the maximum domain dimension. The other parameters are kept the same. In the zoomed in section (Fig. 21b) of the optimized design of Fig. 21a, an elegant design pattern can be seen. Such designs might not only be appreciated by an engineer for being structurally optimal and stable but also by architects due to their aesthetic appeal.

Fig. 21 Converged design for cantilever beam problem solved on Bird tessellation, using a linear filter of radius 3 % of the maximum domain dimension, is shown in (**a**). (**b**) Zoomed in section
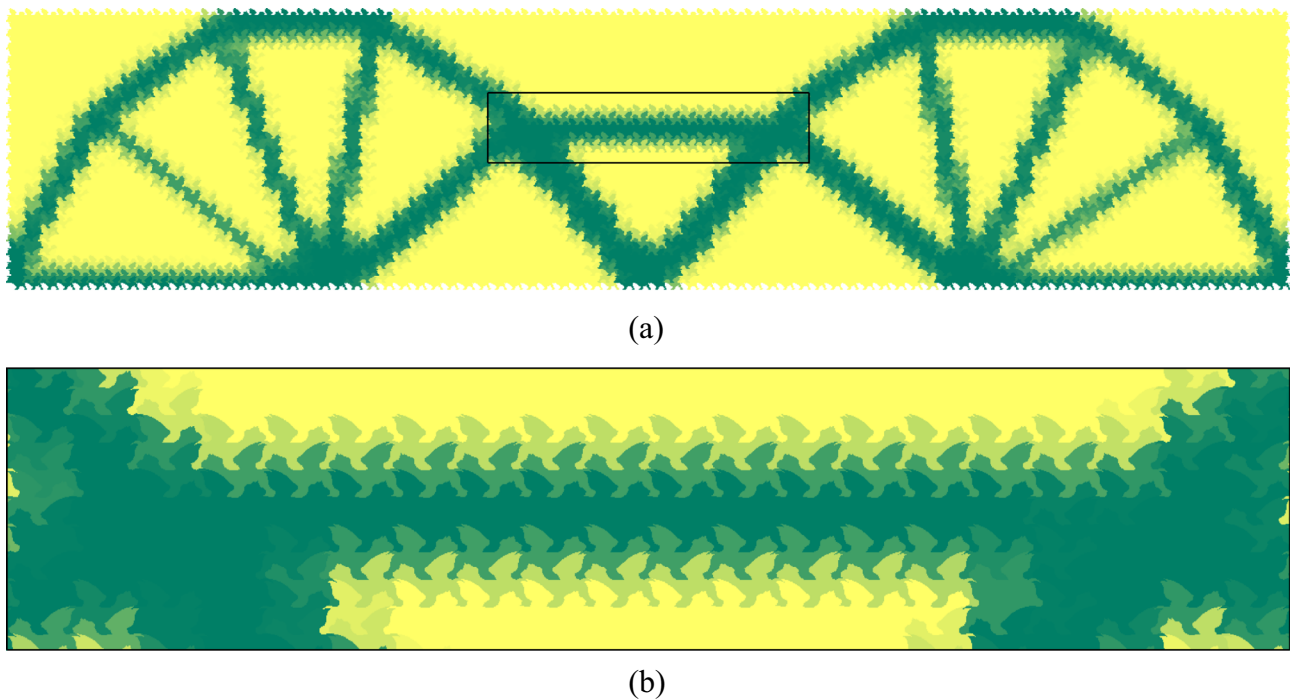

(a)

(b)
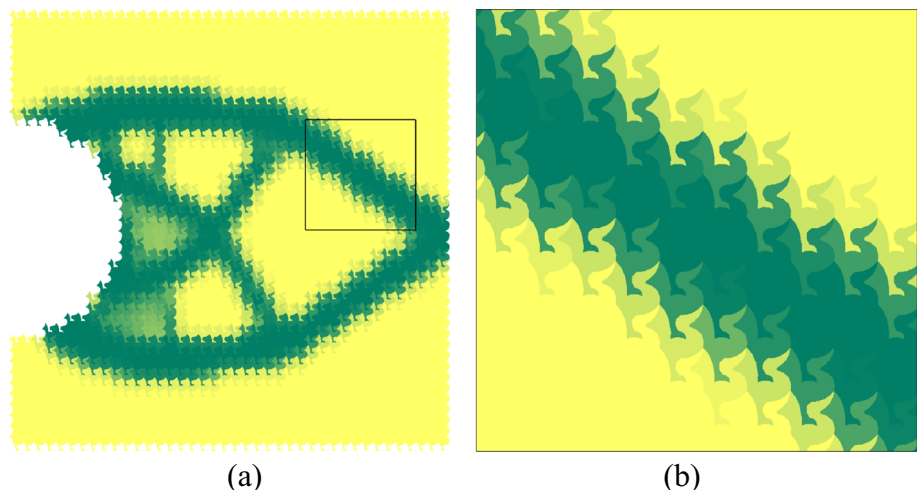
Fig. 22 Bridge problem on Winged Lion tessellation. **(a)** Converged design. **(b)** Zoomed in section

6.3 Bridge problem

Our final example is the optimization of the bridge shown in Fig. 20. The locations of the piers are indicated by pin and roller supports. Two point loads, representing dead weights, are applied at the locations shown in Fig. 20. Escher's type IV^B tessellation - Winged Lion, is used to discretize the design domain. The mesh consists of a total of 3,200 elements and 121,948 nodes. To obtain a graded pattern at the design boundaries, a linear filter of radius equal to 5 % of the minimum domain dimension is used.

The other parameters are kept the same as in previous examples.

The converged design (Fig. 22a) resembles a typical bridge with two fan like structural segments. Figure 22b illustrates the captivating design details at the boundaries. In our opinion, an architect would more often than not choose this design over ones with zigzag boundaries that are typically obtained from topology optimization using typical finite elements such as quadrilaterals. To design bridges with multiple spans, the previously discussed pattern repetition concept can be adopted.

Fig. 23 Architectural designs by Bjarke Ingels Group inspired from the basic shapes such as circles and Voronoi polygons (www.big.dk). **(a)** REN building. **(b)** Warsaw museum of modern art

7 Concluding remarks

In this work, we investigate topology optimization using tessellations as a means to bridge engineering, art and mechanics, and possibly architecture. A special numerical approach is needed to handle tessellations, which can often be highly skewed, degenerate and non-convex in nature. The so-called Virtual Element Method, inspired from the MFD methods, provides an elegant way to handle non self-intersecting closed polygons. This approach does not use shape functions (as classical FEM). In it first the approximation space on each element is split into spaces spanned by linear and higher order polynomials. The discrete bilinear form is constructed to be continuous, bounded and pass the displacement patch test exactly.

We discuss the construction of tessellations, including the ones created using recognizable figures, which are used as the background meshes to generate artistic designs. We make use of compliance minimization topology optimization to obtain our artistic designs, however, other relevant objectives, pertaining to various structural responses, such as minimization of lateral drift, maximization of the fundamental eigenvalue and maximization of the minimum critical buckling load Bendsøe and Sigmund 2003 may be used and will be the topic of future investigations.

We obtain optimal designs that might be appreciated by both engineers, who are concerned with structural stability and efficient load transfer, and architects, who focus on style, aesthetics and appearance. In this context, we remark that architectural firms such as Bjarke Ingels Group have been using basic shapes such as circles and Voronoi polygons (c.f. Fig. 23) in their designs. We hope that our approach of topology optimization using tessellations acts as a source of inspiration for architects and engineers alike who are willing to challenge the status-quo in order to create new innovative designs.

Nomenclature

Ω	topology optimization design domain
a, a_h	continuous and discrete bilinear form
f	continuous load linear form
$\mathcal{V}, \mathcal{V}_h$	continuous and conforming discrete solution space
C	elasticity tensor
$\epsilon(\cdot)$	symmetric gradient operator
t	surface tractions
$\mathcal{W}$	space of finite dimensional smooth functions over element e
a^e, a_h^e	restriction of a, a_h to $\mathcal{W}$ (element contribution)
s^e	approximate bilinear form for higher-order deformation modes
φ_i	generic barycentric coordinates
$\boldsymbol{\varphi}_i$	canonical basis function
$\overline{v}$	mean of values of v sampled over the vertices of element e
$\langle v \rangle$	area average of v
$\mathcal{P}$	space of linear deformation modes
p_i	bases spanning space $\mathcal{P}$
$\pi_{\mathcal{P}}$	projection map to extract $\mathcal{P}$, $\pi_{\mathcal{P}} : \mathcal{W} \to \mathcal{P}$
$P_{\mathcal{P}}$	matrix representation of $\pi_{\mathcal{P}}$
$W_{\mathcal{P}}$	matrices containing line integration quantities
$N_{\mathcal{P}}$	matrices containing rearranged nodal coordinates of vertices
q_i	vector of line integration of barycentric coordinates
K_e	element stiffness matrix
D	material matrix which is function of elasticity tensor C
I	identity matrix
α^e	positive scaling coefficient for stability term s^e
J	objective function
V_f	prescribed volume fraction
ρ, ρ_e	continuous density function and discrete element density
C^0	elasticity tensor of the solid region
K	global stiffness matrix
F	global force vector
U	global displacement vector
$\lvert \cdot \rvert$	measure of a set (area) or Euclidean norm of vector
E	Young's modulus
ν	Poisson's ratio
σ	stress tensor
e_u	displacement error
e_σ	stress error

References

Escher MC The official website. http://www.mcescher.com/

Almeida SRM, Paulino GH, Silva ECN (2010) Layout and material gradation in topology optimization of functionally graded structures: A global-local approach. Struct Multidiscip Optim 42(6):855–868

Arroyo M, Ortiz M (2006) Local maximum-entropy approximation schemes: a seamless bridge between finite elements and meshfree methods. Int J Numer Methods Eng 65(13):2167–2202

Barber JR (2010) Elasticity , 3rd edn. Springer, Berlin Heidelberg New York

Beghini LL, Beghini A, Katz N, Baker WF, Paulino GH (2014) Connecting architecture and engineering through structural topology optimization. Eng Struct 59:716–726

Beirão Da Veiga L, Brezzi F, Cangiani A, Manzini G, Marini LD, Russo A (2013a) Basic principles of virtual element

methods. Math Model Methods in Appl Sci 23(1):199–214

Beirão Da Veiga L, Brezzi F, Marini LD (2013b) Virtual elements for linear elasticity problems. SIAM J Numer Anal 51(2):794–812

Beirão Da Veiga L, Brezzi F, Marini LD, Russo A (2013c) The hitch-hiker guide to the virtual element Method. Math Model Methods in Appl Sci:1–32

Beirão Da Veiga L, Manzini G (2013) A virtual element method with arbitrary regularity. IMA J Numer Anal:1–23. doi:10.1093/imanum/drt018

Belikov VV, Ivanov VD, Kontorovich VK, Korytnik SA, Semenov AY (1997) The Non-sibsonian interpolation: A new method of interpolation of the values of a function on an arbitrary set of points. Comput Math Math Phys 37(1):9–15

Bendsøe MP (1989) Optimal shape design as a material distribution problem. Struct Optim 1:193–202

Bendsøe MP, Kikuchi N (1988) Generating optimal topologies in structural design using a homogenization method. Comput Methods Appl Mech Eng 71(2):197–224

Bendsøe MP, Sigmund O (2003) Topology optimization - Theory, methods and applications. Springer, New York

Bishop JE (2009) Simulating the pervasive fracture of materials and structures using randomly close packed Voronoi tessellations. Comput Mech 44(4):455–471

Bolander JE, Saito S (1998) Fracture analysis using spring networks with random geometry. Eng Fract Mech 61:569–591

Bolander JE, Sukumar N (2005) Irregular lattice model for quasistatic crack propagation. Phys Rev B- Condens Matter Mater Phys 71(9). art. no. 094106

Bool FH, Kist JR, Wierda F, Locher JL (1992) M.C. Escher: His life and complete graphic work. Harry N. Abrams, Inc, New York

Brezzi F, Marini LD (2013) Virtual Element Methods for plate bending problems. Comput Methods Appl Mech Eng 253:455–462

Christ NH, Friedberg R, Lee TD (1982) Weights of links and plaquettes in a random lattice. Nucl Phys B 210(3):337–346

Christensen PW, Klarbring A (2008) An introduction to structural optimization. Springer, Berlin Heidelberg New York

Cook RD, Malkus DS, Plesha ME, Witt RJ (2002) Concepts and applications of finite element analysis. John Wiley and Sons, Inc, New Jersey

Emmer M, Schattschneider D (eds) (2005) M.C. Escher's legacy: A centennial celebration. In: Emmer M, Schattschneider D (eds). Springer, Berlin Heidelberg New York

Fathauer R (2010) Designing and drawing tessellations. Tessellations

Fathauer R (2011) Fractal trees. Tarquin Publications

Floater MS (2003) Mean value coordinates. Comput Aided Geom Des 20(1):19–27

Floater MS, Hormann K, Kòs G (2004) A general construction of barycentric coordinates over convex polygons. Adv Comput Math 24(1-4):311–331

Floater MS, Kòs G, Reimers M (2005) Mean value coordinates in 3D. Comput Aided Geom Des 22(7):623–631

Gain AL, Paulino GH (2012) Phase-field based topology optimization with polygonal elements: A finite volume approach for the evolution equation. Struct Multidiscip Optim 46(3):327–342

Gain AL, Paulino GH, Leonardo D, Menezes IFM (2013) Topology optimization using polytopes. Submitted. arXiv:1312.7016

Gain AL, Talischi C, Paulino GH (2014) On the virtual element method for three-dimensional elasticity problems on arbitrary polyhedral meshes. Comput Methods Appl Mech Eng. In press. doi:10.1016/j.cma.2014.05.005

Ghosh S (2011) Micromechanical analysis and multi-scale modelling using the voronoi cell finite element method. CRC Press, Boca Raton

Groenwold AA, Etman LFP (2008) On the equivalence of optimality criterion and sequential approximate optimization methods in the classical topology layout problem. Int J Numer Methods Eng 73(3):297–316

Hassani B, Hinton E (1999) Homogenization and structural topology optimization: Theory, practice and software. Springer, Berlin Heidelberg New York

Hiyoshi H, Sugihara K (1999) Two generalizations of an interpolant based on Voronoi diagrams. Int J Shape Model 5(2):219–231

Hormann K, Sukumar N (2008) Maximum entropy coordinates for arbitrary polytopes In: Eurographics symposium on geometry processing, vol 27, pp 1513–1520

Hormann K, Tarini M (2004) A quadrilateral rendering primitive In: Proceedings of the siggraph/eurographics workshop on graphics hardware, pp 7–14

Mijar AR, Swan CC, Arora JS, Kosaka I (1998) Continuum topology optimization for concept design of frame bracing systems. J Struct Eng 124(5):541–550

Natarajan S, Bordas S, Mahapatra DR (2009) Numerical integration over arbitrary polygonal domains based on Schwarz-Christoffel conformal mapping. Int J Numer Methods Eng 80(1):103–134

Ohsaki M (2010) Optimization of finite dimensional structures. CRC Press, Boca Raton

Papoulia KD, Vavasis SA, Ganguly P (2006) Spatial convergence of crack nucleation using a cohesive finite-element model on a pinwheel-based mesh. Int J Numer Methods Eng 67(1):1–16

Paulino GH, Park K, Celes W, Espinha R (2010) Adaptive dynamic cohesive fracture simulation using nodal perturbation and edge-swap operators. Int J Numer Methods Eng 84(11):1303–1343

Penrose R (1979a) Pentaplexity a class of non-periodic tilings of the plane. The Math Intell 2(1):32–37

Penrose R (1979b) Set of tiles for covering a surface. U.S. Patent 4133152

Rozvany GIN, Zhou M, Birker T (1992) Generalized shape optimization without homogenization. Struct Multidiscip Optim 4(3-4):250–252

Schattschneider D (2004) M.C. Escher: Visions of symmetry, 2nd edn. Harry N. Abrams

Sibson R (1980) A vector identity for the Dirichlet tessellation. Math Proc Camb Philos Soc 87:151–155

Sukumar N (2004) Construction of polygonal interpolants: A maximum entropy approach. Int J Numer Methods Eng 61(12):2159–2181

Sukumar N, Malsch EA (2006) Recent advances in the construction of polygonal finite element interpolations. Arch Comput Methods Eng 13(1):129–163

Sukumar N, Moran B, Semenov AY, Belikov VV (2001) Natural neighbor Galerkin methods. Int J Numer Methods Eng 50:1–27

Sukumar N, Tabarraei A (2004) Conforming polygonal finite elements. Int J Numer Methods Eng 61(12):2045–2066

Suzuki K, Kikuchi N (1991) A homogenization method for shape and topology optimization. Comput Methods Appl Mech Eng 93(3):291–318

Svanberg K (1987) The method of moving asymptotes - a new method for structural optimization. Int J Numer Methods Eng 24(2):359–373

Talischi C, Paulino GH, Pereira A, Menezes IFM (2010) Polygonal finite elements for topology optimization: A

unifying paradigm. Int J Numer Methods Eng 82:671–698

Talischi C, Paulino GH, Pereira A, Menezes IFM (2012) PolyTop: A matlab implementation of a general topology optimization framework using unstructured polygonal finite element meshes. J Struct Multidiscip Optim 45(3):329–357

Timoshenko SP, Goodier JN (1970) Theory of elasticity, 3rd edn. McGraw Hill, New York

Wachspress EL (1975) A rational finite element basis. Academic Press, New York

Warren J (1996) Barycentric coordinates for convex polytopes. Adv Comput Math 6(1):97–108